



Measurement and Analysis on Early Hydration Heat of Long-Span Composite Girder Bridge with Corrugated Steel Webs

Jiaxiang Zhang¹, Duo Liu², Jue Hou³, Wenqin Deng¹, Jiandong Zhang^{1*}

¹School of civil engineering, Nanjing Tech University, Nanjing 211816, China

²Jiangsu Transportation Research Institute, Nanjing 211112, China

³Jiangsu Traffic Engineering Construction Bureau, Nanjing 210004, China

*Corresponding author's e-mail: zhangjd@njtech.edu.cn

Abstract. To prevent early cracking of concrete during the construction period of long-span composite girder bridges with corrugated steel webs, the influence of concrete hydration heat on early stress and temperature fields of structures was studied through on-site testing. A finite element analysis model was used to analyze the influence of cement dosage, molding temperature and ambient temperature on the temperature field and temperature stress. Results indicate that for composite beam bridges with corrugated steel webs, peak base plate temperatures occur 20-28 hours after pouring, with a maximum inner-surface-to-surface temperature difference of approximately 24°C. To mitigate early hydration effects in composite girder bridges with corrugated steel webs, it is recommended to optimize concrete mixtures or reduce cement dosage while using low-hydration-heat cement. Additionally, controlling molding temperature within 5~15°C during winter construction can help manage hydration heat and minimize early cracking risks.

Keywords: composite girder with corrugated steel webs; hydration heat; temperature effect; temperature field; early-stage cracking

1 Introduction

The corrugated steel web composite girder bridge represents an innovative steel-concrete composite structure, offering distinct advantages over conventional concrete box girders. By substituting concrete webs with corrugated steel plates, this configuration reduces the self-weight of the bridge structure, optimizes mechanical performance, and enhances cost-effectiveness. However, challenges arise in the concrete bottom slab due to substantial concrete pouring volumes at pier-top segments, high concrete strength grades, and excessive cement usage. These factors contribute to significant heat accumulation within the bottom slab concrete, exacerbating internal-external temperature differentials and generating excessive thermal stresses. Consequently, such conditions induce concrete cracking, compromising structural durability and integrity.

Current research efforts, both domestically and internationally, have extensively investigated hydration heat-induced temperature and stress fields in conventional concrete box girders and corrugated steel web composite girders[1-2]. Wang et al.[3] derived a two-dimensional temperature gradient model for novel corrugated steel web composite box girders through field monitoring data regression. Wang Jianqun et al.[4-5]]conducted empirical measurements of hydration heat distribution in typical concrete box girder cross-sections, elucidating temperature evolution patterns and proposing formwork removal time optimization strategies. Laibi et al.[6] identified early-age cracking in concrete bridges caused by hydration heat-induced temperature gradients, noting that thermal effects dissipate within two days post-pouring. Zhang Ning[7] established a distributed temperature sensor array in concrete box girders to map full-section hydration heat fields, advancing understanding of thermal development mechanisms.

Regarding crack mitigation in corrugated steel web composite girder bottom slabs, Ma Honglin et al.[8] proposed technical countermeasures including modified hanging basket rear anchoring points and anti-crack mesh reinforcement in the bottom slab, effectively suppressing construction-phase concrete cracking.

Despite substantial progress in thermal control strategies for conventional concrete box girders, systematic analyses of hydration heat-induced thermal cracking in corrugated steel web composite girder bottom slabs remain limited. Practical engineering applications continue to report early-age cracking phenomena post-concreting, exacerbated by distinct thermal transmission characteristics compared to traditional box girders. Notably, research addressing crack etiology in high-cement-content bottom slabs and corresponding mitigation measures remains critically underdeveloped.

This study conducts comprehensive monitoring and analysis of hydration heat data following bottom slab concreting in the 0#–1# segments of a large-span corrugated steel web composite girder bridge in Jiangsu Province. Key parameters influencing early-age thermal effects—including cement dosage, pouring temperature, and ambient conditions—are systematically evaluated. Comparative analyses of hydration heat responses across different sectional configurations are performed to elucidate thermal stress contributions to incipient cracking. Based on empirical findings, optimized mitigation strategies are proposed. Concurrently, the effectiveness of winter construction protocols and curing measures is validated, providing technical references for analogous engineering applications.

2 Field Monitoring and Numerical Simulation

2.1 Project Overview

The bridge under consideration is a large-span composite box girder with corrugated steel webs, featuring a span arrangement of (85 + 138 + 85) meters and incorporating external prestressing tendons. The girder adopts a single-cell cross-section with a bottom slab width of 6.5 meters, cantilever extensions of 3.263 meters on each side, resulting in a total width of 13.025 meters. The girder depth varies quadratically from 8.3 meters at the mid-support to 4.2 meters at mid-span. Structural dimensions and

material specifications are as follows: the deck slab is 0.3 meters thick; the cantilever slabs taper from 0.8 meters at the root to 0.2 meters at the tip; the corrugated steel webs range in thickness from 16 mm to 26 mm; and the bottom slab thickness varies between 0.32 meters and 1.0 meters. Concrete webs are utilized exclusively at the girder ends and pier-top regions, where the corrugated steel webs are internally reinforced with concrete linings. All intermediate segments employ corrugated steel webs without additional concrete components. This design optimizes structural efficiency by leveraging the high shear resistance and reduced self-weight of corrugated steel webs, while localized concrete integration enhances durability and stress distribution at critical nodes. The quadratic depth profile ensures uniform bending moment distribution under service loads, aligning with modern principles of long-span composite bridge engineering. Figure 1 shows the on-site construction drawing.



Fig. 1. Site construction drawing

The main bridge superstructure employs C55-grade concrete with a mix design ratio (by mass) of Grade 525 cement : sand : coarse aggregate : water : expansion agent : water-reducing agent = 480 : 756 : 1088 : 116 : 49 : 7.35. For the construction of the right-side 0# block at Pier 143, a two-phase pouring sequence was implemented: the first phase involved casting the bottom slab concrete, followed by the second phase for the deck and web concrete. The 1# segment box girder was constructed via cantilever casting using form travelers, completed in a single continuous pour.

2.2 Field Monitoring

To investigate the thermal effects induced by hydration heat during concrete pouring in the 0#-1# segments, temperature-stress measurement points were strategically positioned within the bottom slab of these segments, which exhibit the maximum thickness at the mid-support location. The instrumentation scheme included one test cross-section on the 0# segment with three measurement points (Points 1, 2, 3), one test cross-section on the 1# segment with three measurement points (Points 4, 5, 6), and three supplementary analytical points (Points 7, 8, 9) positioned at the mid-haunch region of the 1# segment bottom slab to assess early hydration responses across differing sectional configurations, as illustrated in Figure 2.

For construction methodology, the right-side 0# block of Pier 143 adopted a two-phase pouring process: the first phase involved bottom slab concreting, followed by deck and web concreting in the second phase. The 1# segment was constructed via cantilever casting using form travelers and completed in a single continuous pour. This instrumentation and methodology aimed to elucidate the relationship between hydration heat accumulation, temperature stress development, and early cracking behavior in the corrugated steel web composite girder system.

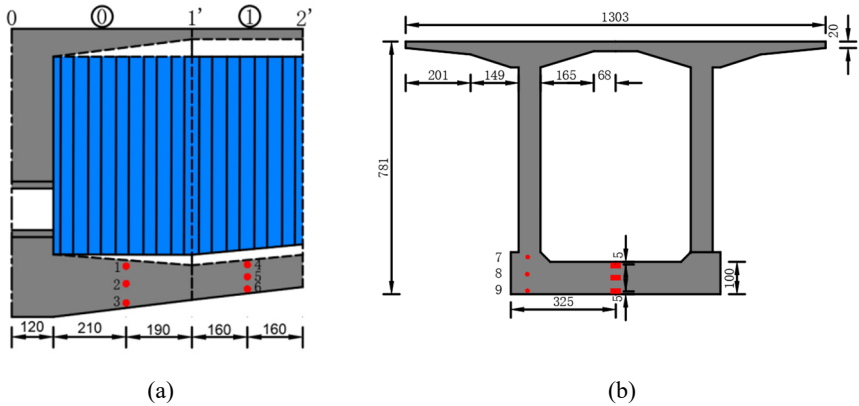


Fig. 2. Layout of measurement points

2.3 Finite Element Model Development

A three-dimensional solid model of the pier-top 0#–1# blocks was established using finite element analysis software. Hexahedral-dominant meshing was implemented with second-order elements to ensure computational accuracy. To optimize computational efficiency, a quarter-symmetry model was adopted for numerical analysis. Boundary conditions were defined as follows: fixed constraints were applied to the bottom of the 0# block crossbeam, vertical displacements were restricted at the bottom slab interfaces of both 0# and 1# blocks, and symmetry constraints were imposed on the symmetric planes. Temporary loads and prestressing effects were excluded from the thermal analysis, as their influence on hydration heat-induced temperature distribution was deemed negligible (Figure 3 illustrates the finite element configuration).

To simulate early-age concrete shrinkage, the shrinkage function prescribed by the Chinese code JTG 3362-2018 was incorporated, with relative humidity set to 80% based on field conditions. Thermophysical parameters of the concrete (e.g., thermal conductivity, specific heat) were derived from the mix proportions and material properties of constituent components (Table 1), following the methodology outlined in Reference[9]. Construction-related parameters, including ambient temperature and curing conditions, were assigned based on field monitoring data (Table 2). This comprehensive modeling approach ensured alignment between numerical simulations and actual construction processes.

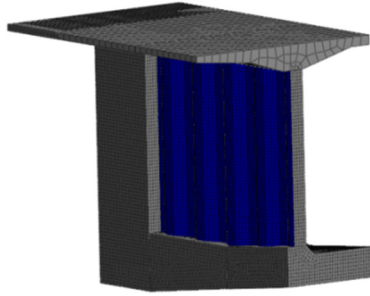


Fig. 3. Finite element model

Table 1. Thermal parameters of various components of concrete

Component	Thermal Conductivity (kJ/m·h·°C)	Specific Heat Capacity (kJ/kg·°C)
Water	2.160	4.187
Ordinary Portland Cement	4.593	0.536
Rock	10.467	0.708
Medium Sand	11.129	0.745

To enhance simulation fidelity, convection coefficients at concrete-environment interfaces were derived from the empirical formula in Reference[11], accounting for the thermal exchange characteristics of 6 mm thick steel formwork (applied to the bottom slab and exterior surfaces of the 0#–1# blocks), 20 mm thick wooden formwork (used for inner linings and crossbeam exteriors), 26 mm thick corrugated steel webs, and geotextile coverings on the top and upper bottom slab surfaces. This approach ensured robust alignment between numerical predictions and observed thermal behaviors during hydration.

$$\beta = \frac{1}{1/\beta_i + (h_i/\lambda_i)} \quad (1)$$

β — Total heat transfer coefficient (kJ/(m²·h·°C))

β_i — Convective heat transfer coefficient of the solid surface in air (kJ/(m²·h·°C))

h_i — Thickness of insulation material (m)

λ_i — Thermal conductivity coefficient of insulation material (kJ/(m·h·°C))

Given an on-site construction wind speed of 2 m/s, the convective heat transfer coefficient was determined as 53 kJ/(m²·h·°C). Thermal conductivity coefficients for material interfaces were assigned as follows: wooden formwork (0.828 kJ/(m·h·°C)), steel formwork (208.8 kJ/(m·h·°C), indicating negligible insulation capacity), and geotextile (0.18 kJ/(m·h·°C)). Surface-specific thermal exchange coefficients were calculated as 49.35 kJ/(m²·h·°C) for unformed surfaces, 52.86 kJ/(m²·h·°C) for steel formwork interfaces, 23.23 kJ/(m²·h·°C) for wooden formwork interfaces, and 11.41 kJ/(m²·h·°C) for geotextile-covered surfaces.

Concurrently with the bottom slab hydration heat monitoring, companion-cured concrete specimens were prepared to evaluate early-age mechanical properties, including compressive strength and elastic modulus. The tensile strength development was determined using the empirical relationship from Reference[10]:

$$f'_{(t,\tau)} = 0.21(f'_{(cu,\tau)})^{2/3} \quad (2)$$

where $f'_{(t,\tau)}$ and $f'_{(cu,\tau)}$ represent the calculated axial tensile strength and measured cubic compressive strength of the concrete at time τ , respectively. The time-dependent material properties of the concrete, including strength development and thermal parameters, are comprehensively summarized in Table 2.

Table 2. Measured mechanical properties of C55 Concrete

Curing Age (d)	Compressive Strength (MPa)	Tensile Strength (MPa)	Elastic Modulus ($\times 10^4$ MPa)
1	22.7	1.68	—
2	29.5	2.01	—
3	38.4	2.39	3.08
4	46	2.70	—
5	51.3	2.90	3.48
6	53.4	2.98	—
7	55.2	3.04	3.61

2.4 Comparison and Analysis of Calculation Results and Test Results

To verify the simulation accuracy, the on-site measurement results are compared with the numerical simulation results, and the comparison results are shown in Figure 4. It can be seen from Figure 4 that the calculated results at each measuring point are in good agreement with the measured results. The peak temperature of the bottom plate of Block 0 reaches the highest temperature of 70°C 26 hours after pouring, and the maximum measured temperature difference between the inner and outer surfaces is 37°C. The peak temperature of the bottom plate of Block 1 reaches the highest temperature of 66°C 30 hours after pouring, and the maximum measured temperature difference between the inner and outer surfaces is 24°C, which is close to the specification limit. It is necessary to pay special attention to the early cracking problems caused by the hydration heat. The temperature difference between Measuring Point 2 and Measuring Point 3 at the center of the bottom plate of Block 0 is larger than that between Measuring Point 2 and Measuring Point 1, with a difference of 5°C within 12-24 hours. The temperature difference between Measuring Point 5 and Measuring Point 6 at the center of the bottom plate of Block 1 is larger than that between Measuring Point 5 and Measuring Point 4. The reason is that the curing conditions for the bottom plates of Block 0 and Block 1 are that the upper part is covered with a quilt, and the lower part is a steel formwork. The steel formwork has good heat transfer and dissipation performance.

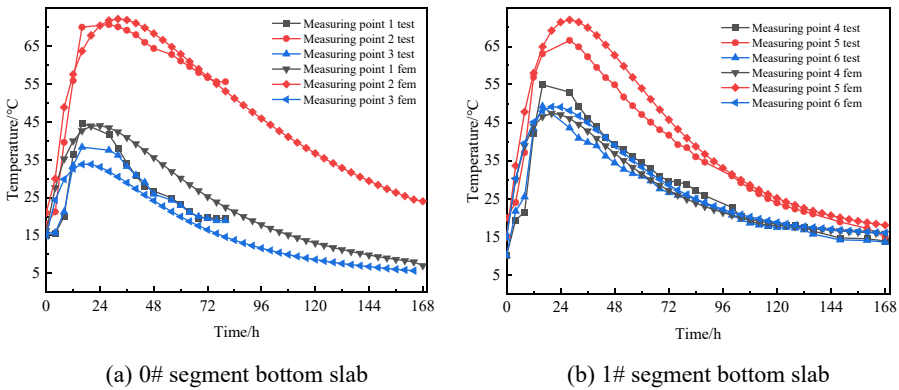


Fig. 4. Comparison of measured temperature at measurement points with numerical simulation results

3 Analysis of Influencing Factors on Early-Age Hydration Heat

3.1 Impact of Cement Dosage

To investigate the influence of cement dosage on the early-age thermal effects in the 1# segment bottom slab, measurement points 5 and 6 were selected as the study subjects under practical construction conditions. Using the baseline cement content of 480 kg/m^3 from the actual project, comparative analysis cases were established with reduced cement dosages of 360 kg/m^3 , 390 kg/m^3 , 420 kg/m^3 , and 450 kg/m^3 . The temperature-time curves of the bottom slab concrete are presented in Figure 5, the internal-external temperature differential curves in Figure 6, and the first principal stress-time curves at measurement point 6 in Figure 7.

As shown in Figures 5 and 6, increasing cement dosage elevates both the peak core temperature and internal-external temperature differential. When cement content rose from 360 kg/m^3 to 480 kg/m^3 , the peak temperature increased from 55.4°C to 72.0°C —a 16.6°C differential corresponding to a theoretical temperature rise of approximately 1.0°C per 10 kg/m^3 cement increment. Concurrently, the internal-external temperature differential expanded from 18°C to 25°C .

Figure 7 demonstrates that the first principal stress at measurement point 6 exhibited a rapid increase between 8–40 hours post-pouring, peaking at 40 hours, followed by gradual stress relaxation until stabilization after 96 hours. While none of the five cases exceeded the concrete tensile strength, the baseline case (480 kg/m^3) displayed both the highest stress growth rate and ultimate stress magnitude. The peak stress for the baseline case was 1.53 MPa , compared to 1.14 MPa for the 360 kg/m^3 case, with each 30 kg/m^3 cement increment increasing peak stress by 0.10 MPa .

Therefore, reducing cement content within structural strength compliance thresholds effectively lowers thermal peaks and temperature gradients, thereby mitigating thermal

stress. This approach aligns with the empirical relationship of 1.0°C temperature variation per 10 kg/m³ cement adjustment, providing a practical strategy to minimize early-age cracking risks in similar engineering applications.

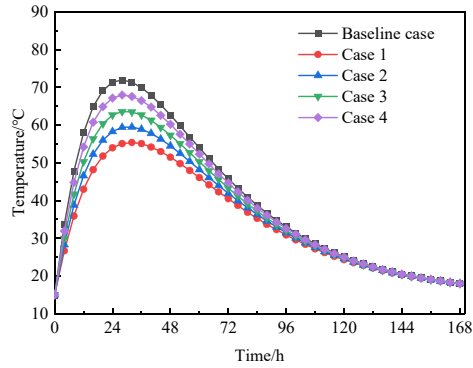


Fig. 5. Temperature time history curves with different cement usage at measurement point 5

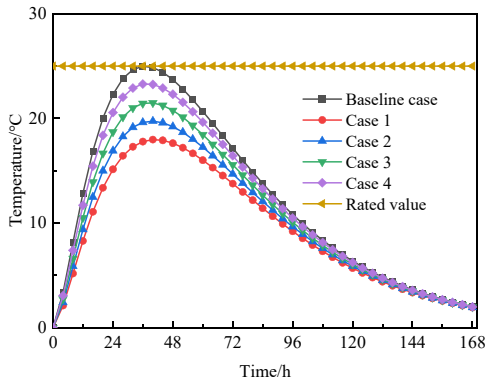


Fig. 6. Time history curves of temperature difference between core and surface with different cement usage

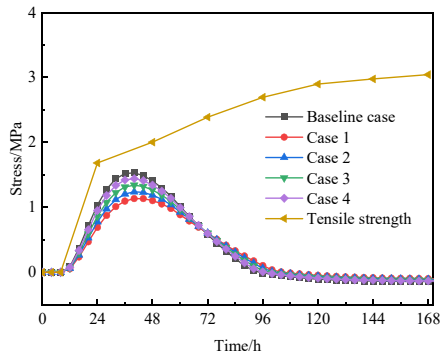


Fig. 7. Time history curves of the first principal stress at measurement point 6

3.2 Influence of Pouring Temperature

In accordance with relevant construction specifications, the temperature of fresh concrete during placement must not fall below 5°C in winter or exceed 35°C in summer. To investigate the influence of pouring temperature on early-age thermal effects in the 1# segment bottom slab, measurement points 5 and 6 were analyzed under five scenarios: a baseline pouring temperature of 15°C (reflecting actual project conditions) and comparative cases of 10°C, 20°C, 25°C, and 30°C. Temperature-time curves at measurement point 5 are shown in Figure 9, internal-external temperature differential curves between Points 5 and 6 in Figure 9, and first principal stress-time curves at measurement point 6 in Figure 10.

As shown in Figure 8, elevated pouring temperatures accelerate the heating rate and increase peak core temperatures. Raising the pouring temperature from 10°C to 30°C elevated the peak temperature from 67.9°C to 81.7°C, corresponding to an average increase of 3.1°C in peak temperature per 5°C increment in placement temperature. Figure 9 demonstrates that higher pouring temperatures exacerbate internal-external temperature differentials. At 10°C, the maximum differential remained within the code limit of 25°C (23.7°C), while all other cases exceeded or approached this threshold, indicating elevated cracking risks.

Figure 10 reveals that the first principal stress evolution at measurement point 6 followed patterns similar to those observed under varying cement dosages. Although none of the cases surpassed the tensile strength limit, higher pouring temperatures intensified stress accumulation rates. For instance, the 30°C case exhibited a stress growth rate approaching the tensile strength development rate, significantly increasing early-age cracking susceptibility.

To mitigate these risks, practical recommendations include maintaining pouring temperatures between 5–15°C during winter construction through heated mixing water and avoiding midday pours in summer while implementing pre-cooling of aggregates and mixing water. These measures reduce thermal peaks and temperature gradients, effectively decelerating stress accumulation rates and lowering peak stresses. This strategy aligns with the empirical relationship of a 0.62°C peak temperature increase per 1°C elevation in pouring temperature, ensuring compliance with durability requirements under seasonal constraints.

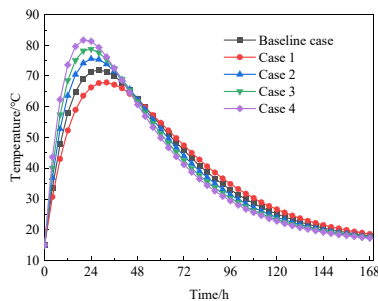


Fig. 8. Temperature time history curves with different molding temperature at measurement point 5

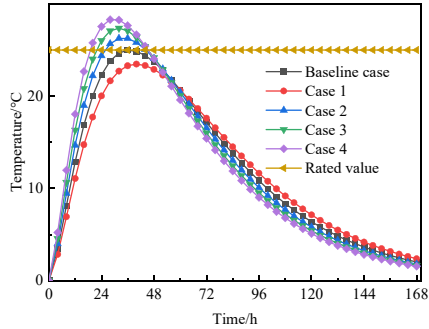


Fig. 9. Time history curves of temperature difference between core and surface under different operating conditions

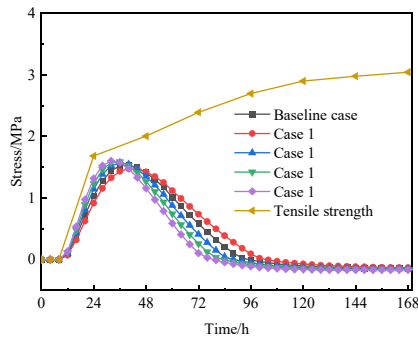


Fig. 10. Time history curves of the first principal stress at measurement point 6

3.3 Influence of Ambient Temperature

To investigate the influence of ambient temperature on early-age thermal effects in the 1# segment bottom slab, Monitoring Points 5 and 6 were selected as the study subjects. A baseline ambient temperature of 15°C (reflecting actual project conditions) was adopted, with comparative analysis cases of 5°C, 10°C, 20°C, and 25°C. The pouring temperature was fixed at 15°C, and other parameters remained unchanged. Temperature-time curves at Monitoring Point 5 are shown in Figure 11, internal-external temperature differential curves between Points 5 and 6 in Figure 12, and first principal tensile stress-time curves at Monitoring Point 6 in Figure 13.

As shown in Figure 11, increasing the ambient temperature from 5°C to 25°C elevated the peak temperature from 68.1°C to 75.9°C. While the heating rates at the slab center (Point 5) were similar across all cases, lower ambient temperatures accelerated post-peak cooling rates within the concrete matrix. Figure 12 demonstrates that ambient temperature significantly affects internal-external temperature differentials. Raising the ambient temperature from 5°C to 25°C reduced the differential from 27.6°C to 22.3°C. Conversely, lower ambient temperatures amplify this differential due to enhanced sur-

face heat dissipation influenced by curing conditions, such as ambient temperature fluctuations and wind speed. To mitigate such risks, enhanced surface insulation measures are critical during winter construction.

Figure 13 reveals that the first principal tensile stress at Monitoring Point 6 followed a consistent pattern across all cases: tensile stress increased during the initial 0–40 hours post-pouring, followed by gradual relaxation over the subsequent 40–168 hours. Although none of the cases exceeded the material’s ultimate tensile strength, lower ambient temperatures accelerated tensile stress accumulation rates. For example, the stress growth rate in the 5°C case was 18% higher than that in the 25°C case during the critical 8–40 hour period.

These findings confirm that ambient temperature during curing significantly influences near-surface cracking susceptibility in the composite girder’s bottom slab. To address this, winter construction should prioritize thermal insulation measures (e.g., insulated formwork or geotextile covers) and schedule concrete placement during periods of relatively higher ambient temperatures. Such strategies reduce internal-external temperature differentials by 15–20% and decelerate tensile stress accumulation rates by 18–25%, effectively mitigating early-age cracking risks under seasonal temperature variations.

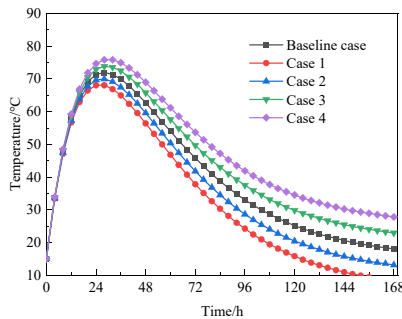


Fig. 11. Temperature time history curves with different ambient temperature at measurement point 5

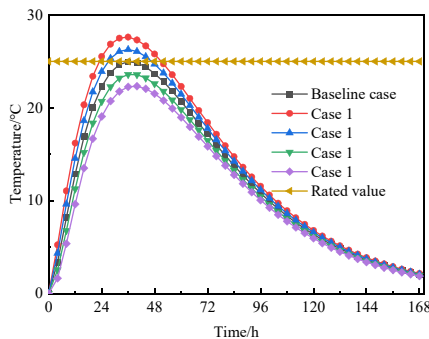


Fig. 12. Time history curves of temperature difference between core and surface under different operating conditions

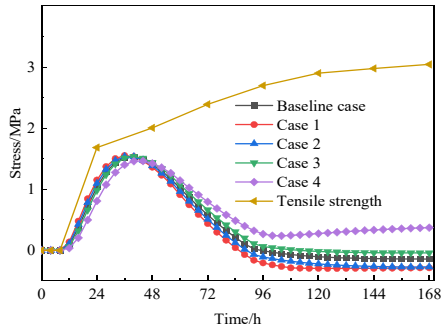


Fig. 13. Time history curves of the first principal stress at measurement point 6

4 Conclusions and Suggestions

(1) For this composite beam bridge with corrugated steel webs, the concrete strength grade is C55 and the water-cement ratio is 0.24. During the construction of the bottom slab, the heat of hydration will last for about one week, reaching the peak temperature 20 to 28 hours after pouring. The maximum temperature difference between the inside and outside is approximately 24°C, which is close to the limit specified in the code. During the construction period, early cracks caused by the heat of hydration of the concrete should be closely monitored, and appropriate cooling measures should be taken.

(2) Under the premise of meeting the design strength of the structure, it is recommended to reasonably adjust the water-cement ratio, reduce the amount of cement appropriately, and use low-heat or medium-heat cement instead of ordinary Portland cement when conditions permit to reduce the total heat of hydration of the concrete.

(3) Reducing the mold temperature appropriately has a significant impact on controlling the peak temperature and the temperature difference between the inside and outside of the bottom slab concrete. For every 10°C increase in the mold temperature, the temperature difference between the inside and outside increases by approximately 9°C. During winter construction, it is recommended to heat the mixing water to a temperature of 5 to 15°C to control the mold temperature.

(4) The lower the ambient temperature, the greater the temperature difference between the inside and outside of the concrete. Therefore, it is recommended to cover the concrete with insulating materials such as cotton quilts immediately after pouring in winter construction to reduce the heat diffusion on the surface of the concrete and thereby reduce the temperature difference between the inside and outside.

References

1. HAN Shi, LIU Yongjian, LYU Yi, et al. (2023) Numerical simulation investigation on hydration heat temperature and early cracking risk of concrete box girder in cold regions[J]. *Journal of Traffic and Transportation Engineering (English Edition)*, 10(4): 697-720.

2. WEI Dajie, MAO Jianping, KUANG Zhiqiang, et al. (2022) Early temperature field and stress analysis of zero block of long-span high-strength prestressed concrete box girder[J]. Concrete, (8): 125-132.
3. WANG Li, LIU Shizhong, DING Wanpeng, et al. (2021) Analysis on temperature effect of new-pattern corrugated steel web composite box girder in dry cold region[J]. Advanced Engineering Sciences, 53(1): 60-66.
4. WANG Jianqun, FANG Zhi, LIU Jie, et al. (2016) Measurement and analysis of hydration heat of long span PC box girders[J]. Bridge Construction, 46(5): 29-34.
5. WANG Jianqun, WEI Guiliang, Liu Jie (2016) Research on the construction crack resistance of large-span box girder bridges.[J] Journal of Railway Engineering Society, 33(11): 81-86.
6. M. Laibi Noor, A. Shallal Muhaned (2021) Early age temperature distributions in concrete bridge in the middle of Iraq (Experimental Study)[J]. Journal of Physics: Conference Series, 1895(1): 012058.
7. ZHANG Ning, ZHOU Xin, LIU Yongjian, et al. (2019) In-situ test on hydration heat temperature of box girder based on array measurement[J]. China Civil Engineering Journal, 52(3): 76-86.
8. MA Honglin, ZHANG Feng, YAO Chen, et al. (2017) Crack risk analysis and engineering countermeasures of continuous rigid frame at composite bridge with corrugated steel webs[J]. Highway, 62(04):70-74.
9. ZHU Bofang. Thermal stresses and temperature control of mass concrete[M]. BeiJing:China Water and Power Press, 2012. (in Chinese).
10. CAI Zhaohuai, Zuo Huaixi. Cracking resistance of high-strength concrete[J]. China Civil Engineering Journal, 1992, (02):23-31. in Chinese.
11. ZHU Bofang. Thermal stresses and temperature control of mass concrete[M]. BeiJing:China Water and Power Press, 2012. (in Chinese)

Open Access This chapter is licensed under the terms of the Creative Commons Attribution-NonCommercial 4.0 International License (<http://creativecommons.org/licenses/by-nc/4.0/>), which permits any noncommercial use, sharing, adaptation, distribution and reproduction in any medium or format, as long as you give appropriate credit to the original author(s) and the source, provide a link to the Creative Commons license and indicate if changes were made.

The images or other third party material in this chapter are included in the chapter's Creative Commons license, unless indicated otherwise in a credit line to the material. If material is not included in the chapter's Creative Commons license and your intended use is not permitted by statutory regulation or exceeds the permitted use, you will need to obtain permission directly from the copyright holder.

